EUROPEAN ORGANIZATION FOR NUCLEAR RESEARCH

CERN-PPE/90-164
7 November 1990

Backward Production of Mesons Associated with $\Delta^{++}(1232)$ in π^+p interactions at 20 GeV/c

V.F.Perepelitsa[4], N.Z.Akopov[1], L.Dorsaz[2], A.Ferrer[3], A.A.Grigoryan[1], V.V.Karapetyan[1], V.I.Mikhailichenko[4], S.Ya.Nikitin[4], P.Sonderegger[2], A.S.Zhokin[4].

Abstract

We have analyzed backward meson production in π^+p reactions at 20 GeV/c, which were measured in the CERN Ω spectrometer triggered by a fast proton (p_f), in experiment WA56. Production via baryon exchange of quasi-two-body final states $\Delta^{++}(1232)$ $\rho^0(770)$, $\Delta^{++}(1232)$ $f_2(1270)$ and $\Delta^{++}(1232)$ $\rho_3^0(1690)$ is clearly identified. The density matrix elements of meson resonances and of $\Delta^{++}(1232)$ are analyzed. We have observed also the reactions $\pi^+p \to \Delta^{++}(1232)\pi^0$ and $\pi^+p \to \Delta^{++}(1232)$ ω in the $p_f\pi^+\pi^0$ and $p_f\pi^+\pi^+\pi^-\pi^0$ final states.

1. Yerevan Physics Institute, Br. Alikhanian st. 2, 375036 Yerevan, Armenia
2. CERN, 1211 Geneva 23, Switzerland
3. IFIC, Univ. of Valencia - CSIC. 46100 Burjasot, Valencia, Spain
4. Institute of Theoretical and Experimental Physics, 117 259 Moscow, USSR.

1. Introduction

The production of meson and baryon resonances via baryon exchange has not been extensively studied at high energies. There are no experimental data on such reactions at beam momenta exceeding 16 GeV/c [1]. Doing such experiments at high energy is important in two respects. Firstly, the mechanisms responsible for resonance production (such as the role of baryon Regge-trajectories, the contribution of moving cuts, etc.) can be clarified. Secondly, the spectroscopy of highly excited resonances can be studied under kinematic conditions which ensure a suitable signal/background ratio.

We report here on the results of the analysis of quasi-two-body reactions

$$\pi^+ p \to \Delta_f^{++}(1232)\ \pi^0 \tag{1}$$

$$\pi^+ p \to \Delta_f^{++}(1232)\ \rho^0(770) \tag{2}$$

$$\pi^+ p \to \Delta_f^{++}(1232)\ f_2(1270) \tag{3}$$

$$\pi^+ p \to \Delta_f^{++}(1232)\ \rho_3^0(1690) \tag{4}$$

$$\pi^+ p \to \Delta_f^{++}(1232)\ \omega\,(783) \tag{5}$$

where Δ_f^{++} stands for a fast forward delta baryon with momentum greater than 15 GeV/c. The data were obtained from the CERN WA56 experiment using the Ω spectrometer [2]. This experiment was originally designed as a high sensitivity search for doubly charged exotic mesons and narrow baryonium states produced via baryon exchange in $\pi^+ p$ interactions at 20 GeV/c [3]. Only part of the WA56 statistics (about 125 events per nanobarn out of a total of 427 events per nanobarn) was available to us.

2. Experimental conditions

The layout of the Ω spectrometer as used in this experiment is shown in Fig. 1. It was designed to enhance the relative yield of baryon exchange reactions with respect to diffractive production of fast forward protons (paired with fast antiprotons). The positively charged beam was focused on a 60 cm long hydrogen target. The incident particles were identified by two Cherenkov counters in the beam. Their momenta and angles were measured by a beam spectrometer and by a set of MWPCs upstream of the target. A 24 element scintillation cylindrical hodoscope ("barrel") surrounding the target and a 1/2 mm pitch wire chamber at its downstream end (Y1 in Fig. 1) provided a measurement of the charged multiplicity. In addition, the barrel information was used to identify the events with slow tracks which were not reconstructed in the off-line treatment.

A set of 32 MWPC planes (type C) and of 30 forward MWPC planes (types B and A in Fig. 1) were used to reconstruct the outgoing charged particles. Two drift chambers (DC1 and DC2) were used to improve the measurement accuracy for the fast particles.

The main trigger requirement was the detection of a fast forward proton with momentum greater than 10 GeV/c. The proton signature was determined with the aid of two multicell atmospheric Cherenkov counters C1 and C2 filled with freon-114 and N_2, respectively, and two scintillation hodoscopes H2 and H3 behind them. The momentum of the trigger proton was computed from three proportional planes (Y0, Y3 and Y4 in Fig. 1) providing a rather sharp momentum cut.

Several multiplicity requirements were imposed: ≥ 1 in the barrel hodoscope, ≥ 1 in Y1, ≥ 2 in the two of them, 2 to 5 in proportional plane Y2 and ≤ 3 in Y3. An antiproton veto provided by the C1-H2 system, suppressed the diffractive events with antiprotons of momenta greater than 2.5 GeV/c. A γ veto consisting of hodoscopes H3 and H4 and a lead sheet of 15 mm thickness in between, eliminated the events with fast π^0.

The geometrical acceptances of the detectors allowed a good efficiency for detecting forward protons with momenta greater than 10 GeV/c. This lower bound ensured an almost complete detection of a fast $\Delta_f^{++}(1232) \rightarrow p_f\pi^+$ in a wide range of $u' = u_{max} - u$, where u is the squared momentum transfer from the incident particle to Δ_f^{++}. The geometrical acceptance of the experiment for the Δ_f^{++} detection in the inclusive reaction $\pi^+p \rightarrow \Delta_f^{++}(1232)$ X is plotted in Fig. 2 as a function of the mass squared M_X^2 and of u'.

3. Selection of events

All events satisfying the requirements of the trigger were processed through the TRIDENT program [4] which reconstructed events geometrically. We then selected three samples of events: two-prong and four-prong charge-balanced events and three-prong events with charge imbalance Δ q = $\pm$ 1. The latter sample was interpreted as coming from four-prong events with the loss of one slow particle not detected by the Ω C-chambers, which did not provide a 4π acceptance. Indeed, when the four-prong sample was processed kinematically, it was found to be almost free of events of reactions (2)-(4). The detection inefficiency due to the loss of one or even two slow particles was confirmed by the Monte Carlo simulation of these reactions. Therefore, the study of reactions (2)-(4) is based mainly on the three-prong and two-prong samples.

An off-line treatment of the C1, C2 Cherenkov counters together with the H2 and H3 hodoscope outputs was used to exclude the contamination by the small number of fast π^+ and K^+ mesons which had escaped identification at the on-line level either by hitting the peripheral Cherenkov cells which were not incorporated in the trigger, or by traversing the Cherenkov counters in the median plane where the mirror edges caused a local inefficiency. In the following analysis, the fastest retained positive track will therefore always be taken as a proton. Furthermore, other secondary particles which had momenta greater than 3 GeV/c and reached the Cherenkov counters, were identified at this stage. Only events which had Cherenkov information compatible with mass hypothesis were retained for further analysis. The event vertex was required to be reconstructed inside the hydrogen target with $\chi^2 \leq 50$. The precision of the momentum reconstruction was 0.1% for the beam particles, 0.3 to 0.5% for the fast proton and 1 to 5% for slow particles.

4. Identification of channels and determination of backward cross sections.

4.1 Three-prong samples

Distributions of the squared missing mass, MM^2, with (p_f, π^+, π^+) and (p_f, π^+, π^-) mass hypotheses for the detected particles of the $+++$ and $++-$ samples are shown in Fig. 3. There is some indication of missed π^- and π^+ signals. However, when we require the barrel element associated with the missing momentum to fire, we obtain the MM^2 distributions shown in Fig. 4 where pion signals are clearly seen. The larger background under the pion peak in the $++-$ sample is due to events of reaction $\pi^+ p \rightarrow p_f p\bar{p}\pi^+$ which dominate this sample (with one slow π^+ lost at the track reconstruction stage).

Having thus inferred the presence of the $p_f\pi^+\pi^+\pi^-$ final state in the 3-prong sample, we retained all those 3-prong events which had MM^2 in the m_π^2 band ($|MM^2 - m_\pi^2| \leq 0.16$ $(GeV/c^2)^2$) and which passed a 1-C kinematic fit with $P(\chi^2) \geq 5\%$. Fig. 5 shows the $M(p_f\pi_1^+)$ vs $M(\pi_2^+\pi^-)$ scatter plot for the reconstructed events, where $\pi_{1(2)}$ stands for the faster (slower) positive pion [1].

An accumulation of events is observed in the $\rho^0(770)$, $f_2(1270)$ and $\rho_3^0(1690)$ regions associated with $\Delta_f^{++}(1232)$.

The invariant mass projections are presented in Fig. 6a for the $p_f\pi_1^+$ system and in Fig. 6b for the $\pi_2^+\pi^-$ system.

Fig. 7a shows the $\pi_2^+\pi^-$ mass, associated with the $\Delta_f^{++}(1232)$, selected by the condition $1.15 < M(p_f\pi_1^+) < 1.31$ GeV/c^2. The strong ρ^0, f_2 and ρ_3^0 signals which are seen in this distribution are the evidence for production of the Δ_f^{++} ρ^0, Δ_f^{++} f_2 and Δ_f^{++} ρ_3^0 states. The last channel, $\pi^+ p \rightarrow \Delta_f^{++}\rho_3^0(1690)$, is observed for the first time in a baryon exchange reaction.

The curves in Figs. 6 and 7 represent parametrizations of the mass spectra of the form:

$$(M - M_0)P_4(M)e^{-M}(1 + BW)$$

where M_0 is a constant equal to the mass threshold, P_4 is a 4th order polynomial and BW is a Breit-Wigner term for the $p_f\pi_1^+$ spectrum and three Breit-Wigner terms for the $\pi_2^+\pi^-$ spectrum respectively. The mass and the width of each Breit-Wigner function were taken from the standard PDG values [5].

The mass distributions observed when requiring that the missing momentum extrapolates to the barrel element which gave a signal turned out to be very similar (not shown). This implies that our procedure of selecting the four-body reaction from the whole data sample is satisfactory and that the background due to an extra π^0 is well suppressed.

We also analyzed the contribution of the π^0 background to our $\Delta_f^{++}\rho^0$, $\Delta_f^{++}f_2$ and Δ_f^{++} ρ_3^0 signals by studying 4-prong events kinematically reconstructed with a missing π^0, and

[1] The $M(p_f\pi_2^+)$ vs $M(\pi_1^+\pi^-)$ scatter plot shows a very weak $\Delta_f^{++}(1232)$ signal and, on the contrary, strong ρ^0 and f_2 signals. We neglect the $\Delta_f^{++}(1232)$ presence in this combination. As for the ρ^0 and f_2 production accompanied by p_f and π_2^+ , a special publication will be devoted to these quasi-three-body reactions.

found that the $\Delta_f^{++}\rho^0$ and $\Delta_f^{++}f_2$ signals from the sample with π^0 (in which the $\Delta_f^{++}\rho_3^0$ signal is absent) are not confused with channels (2)-(4).

Observing Fig. 5 we conclude that the backward production of ρ^0, f_2 and ρ_3^0 is strongly associated with the $\Delta_f^{++}(1232)$. The events with $p\pi_1^+$ masses in two bands adjacent to the central $\Delta_f^{++}(1232)$ interval were used to evaluate the contribution of the background under the $\Delta_f^{++}(1232)$ peak to the ρ^0, f_2, ρ_3^0 signals (Fig. 7b). This was found to be less than 10%.

The samples of events corresponding to each of the three reactions (2)-(4) were defined by imposing the Δ^{++} mass band given above, together with the following mass intervals for the mesons:

$$\rho^0\ (770)\ \ [\ 0.65 < \mathrm{M}(\pi_2^+\ \pi^-) < 0.89\ \mathrm{GeV/c^2}\ ],$$
$$f_2\ (1270)\ [\ 1.13 < \mathrm{M}(\pi_2^+\ \pi^-) < 1.41\ \mathrm{GeV/c^2}\ ],$$
$$\rho_3^0\ (1690)\ [\ 1.53 < \mathrm{M}(\pi_2^+\ \pi^-) < 1.85\ \mathrm{GeV/c^2}\ ].$$

We used the results of our mass fits to estimate the background under each resonance peak. As can be seen from Fig. 7a, the amount of background for each reaction and for the mass bands chosen, ranges from 40% for $\rho^0(770)$ to 50% for ρ_3^0 (1690). A detailed study of the background behaviour was made using those events for which the $\pi_2^+\pi^-$ mass was lying on both sides of the central $\rho^0(770)$, $f_2(1270)$ and $\rho_3^0(1690)$ mass intervals.

4.2 Identification of reaction $\pi^+p \to \Delta_f^{++}\omega$

Reaction (5) leads to the $p_f\pi^+\pi^+\pi^-\pi^0$ final state, which can not be reconstructed kinematically from 3-prong events. However, combining the 4-momentum of the slow detected pion with the total missing momentum, it is possible to reconstruct the total 4-momentum opposite to the Δ_f^{++}. We have analyzed in such a way the events of topology $+++$, where the background coming from $\pi^+p \to p_f p\overline{p}\pi^+$ events is small. The distribution of the squared mass opposite to the Δ_f^{++} shows bumps in the ρ/ω, f_2 and ρ_3 mass regions. To identify the ω signal we have selected the events in which the barrel element intersected by the missing momentum did not give a response.

The distribution of MM^2 opposite to Δ_f^{++} for selected events is shown in Fig. 8a. The invariant mass distribution of the sum of the π_2^+ and the missing system M^- is shown in Fig. 8b. The $\Delta_f^{++}\omega$ signal is clearly seen in these distributions. (Note the absence of visible signals from a_1/a_2 as well as π_2/ω_3 mesons in Fig. 8a). For the following analysis we selected the events with π_2^+ M^- mass between 0.70 and 0.86 $\mathrm{GeV/c^2}$ (80 events of which 40 % are background).

A full kinematical reconstruction of the $p_f\pi^+\pi^+\pi^-\pi^0$ final state was achieved with 4-prong events. Fig. 8c shows the $\pi_2^+\pi^-\pi^0$ mass spectrum of the events which have the $p_f\pi_1^+$ mass in the Δ_f^{++} band. This distribution shows 7 events in the ω mass region.

4.3 Two-prong sample

The distribution of MM^2 with p_f and π^+ mass hypotheses for the two-prong sample with two detected fast positive particles is plotted in Fig. 9. The ρ^0/ω and f_2 bumps are seen in this distribution [2].

The invariant mass of the $p_f\pi^+$ system (Fig. 10a) shows a strong $\Delta_f^{++}(1232)$ signal. Selection of events having the $p_f\pi^+$ mass in the $\Delta_f^{++}(1232)$ band ($1.15 < M(p_f\pi^+) < 1.31$ GeV/c^2) gives the MM^2 distribution shown in Fig. 10b. The ρ^0/ω peak is seen here very clearly, with 500 ± 70 events. This peak includes a contribution from reaction (5), $\pi^+p \rightarrow \Delta_f^{++}(1232)\omega$. which was evaluated at 120 ± 30 events.

We now discuss the $\pi^+p \rightarrow \Delta_f^{++}\pi^0$ reaction (channel (1)). The geometrical acceptance of the apparatus for this channel was high (see Fig. 2), but the triggering probability was suppressed by the WA56 multiplicity conditions (mainly the barrel multiplicity condition $n_{Bar} \geq 1$). These conditions were relaxed for proton momenta above 17 GeV/c, for which events with charged multiplicity ≥ 2 were accepted (two-prong trigger). The resulting acceptance for reaction (1) was relatively small, and did not allow us to observe a clear $\Delta_f^{++}\pi^0$ signal in the presence of a large background of incompletely detected 4-body events. This background was largely suppressed by the cut $p_f \geq 17$ GeV/c applied to the 2-prong sample. Then a weak $\Delta_f^{++}\pi^0$ signal is observed (Fig. 11).

4.4 Geometrical acceptances and integral backward cross sections

To obtain the integral backward cross sections of the observed reactions, a Monte Carlo calculation of the experimental acceptances was carried out. The events of reactions (1)-(5) were generated following the u' distribution extracted from our experimental data analysis given below (see Section 5). The acceptances and cross sections are given in Table 1.

The cross sections correspond to the mass bands of resonances given in Sect.4.1 and are corrected for the unseen decay modes by multiplying by a factor 1.85 for the f_2, 4.2 for ρ_3^0, and 1.1 for the ω.

The satisfactory agreement between the cross sections of reaction $\pi^+p \rightarrow \Delta_f^{++}\rho^0$ as determined from two- and three-prong topologies and reaction $\pi^+p \rightarrow \Delta_f^{++}\omega$ as determined from three- and four-prong topologies, confirms the validity of the computation of the detection efficiencies. Note that the quoted errors in the cross sections are only statistical and do not contain an overall uncertainty of 20% which is mainly due to the accuracy of the acceptance calculations.

[2] No clear signal of backward elastic scattering is seen, due to the very small acceptance of WA56 for this reaction.

4.5 Variation of backward cross section with meson resonance masses.

The most prominent feature of the cross sections quoted in Table 1 is their significant growth with the masses of the meson resonances, from 12 nb for the ω and 29 nb for the $\rho^0(770)$ to 124 nb for the $\rho_3^0(1690)$. A similar behaviour is known for the baryon resonances produced via baryon exchange [6,7].

The backward production of meson resonances presents a special interest from the theoretical point of view. This production is connected to the α_4 trajectory which consists of the two quark and two antiquark pairs and of the two string junctions. This trajectory appears when considering baryon-antibaryon reactions [8]. The cross section for backward production of two-quark states which corresponds to the baryon exchange diagram shown in Fig. 12a, is expressed by the amplitude which has the constituent contents shown in Fig. 12b. For high meson masses the mass dependence of the cross section has the form

$$d^2\sigma/dM^2du = \sum C_{ijk}(u)M^{2(\alpha_{4,i} - \alpha_j - \alpha_k)} \qquad (6)$$

where α_j(u) and α_k(u) are the exchanged baryon trajectories, and C_{ijk}(u) are coefficients. The sum in formula (6) extends over all possible α_4 trajectories and baryon α trajectories.

The question of the existence of the α_4 trajectories is not yet solved. Backward meson production is a useful tool for the investigation of these Regge singularities. A special analysis of our data devoted to the problem of the α_4 trajectory will be carried out in the near future. Note that the formula which describes the backward production of baryons with high masses has the same form as (6), with the α_4 trajectory replaced by the usual quark-antiquark trajectory α_2 with $\alpha_2(0) = 1/2$. The corresponding dual quark diagram is shown in Fig. 12c.

4.6 Energy dependence of total cross sections

In Fig. 13 we show the available integral backward cross sections for $\pi^+p \to \Delta_f^{++}\rho^0$ and $\pi^+p \to \Delta_f^{++}f_2$ reactions. The data points at p_{lab} = 4 GeV/c are taken from [9]. To obtain the points at 8, 9 and 12 GeV/c in Fig. 13b we proceeded as follows. First, we multiplied the data [6,10] for the reaction $\pi^-p \to \Delta^0 f_2$ by the isospin factor 3 (for the reactions πN $\to \Delta f_2$ only isospin 1/2 is allowed in the u-channel). Further, all the data were made to be "homogenous" by taking into account the following corrections: i) the contribution of the tails, assuming Breit-Wigner shaped resonances; ii) since the experiments were done in different intervals of the variable u', we have extrapolated them to the same interval (u' < 1.0 (GeV/c)^2): iii) we have accounted for the branching ratio of $f_2 \to \pi^+\pi^-$ decay (factor 1.85); iv) in addition, the data [6,10] must be multiplied by a factor 3 since the corrections for the $\Delta^0 \to p\pi^-$ decay isospin coefficient were not applied by these authors.

Parametrizing the energy dependence of the cross sections in the form $\sigma_{tot} \approx s^{-n}$ we see that n ranges from 3 to 4. This is in agreement with the energy dependence of the N_α Regge

trajectory contribution.

5. Differential cross sections

We have analyzed the differential cross sections for the reactions (1) - (5). Fig. 14 shows the $d\sigma/du'$ distributions for these reactions.

The distributions given have been corrected for the u' dependent acceptance. using a Monte Carlo simulation. The decay angular distributions of resonances used in the Monte Carlo generation of reactions (2) - (5) were extracted from our experimental analysis (see Section 6). As to the reaction (1). isotropic $\Delta_f^{++}(1232)$ decay was assumed.

We have fitted the u' distributions using the exponential form $d\sigma/du' = A \exp(-bu')$. The resulting slopes are given in Table 1, the fitted curves are drawn in Fig. 14.

6. Density matrices

A detailed study of $\Delta_f^{++}, \rho^0, f_2$ and ρ_3^0 decay angular distributions in the Jackson frame was performed with a quasi-two-body Monte Carlo simulation program, into which we incorporated the trigger efficiency and the Ω detector efficiency and acceptance. We infer that no strong bias is expected in Δ_f^{++} decay angular distributions, except for reaction (1) which is identified by the cut $p_f > 17$ GeV/c.

On the other hand. the meson decay angular distributions are strongly affected by the Ω geometrical acceptance. It is possible, however, to compensate to a great extent the rapid acceptance variations by summing the angular distributions from both three-prong topologies: $+++$ and $++-$ (after appropriate background subtraction). These topologies are complementary since they come from $\Delta_f^{++}\pi_2^+$ (π^-) and $\Delta_f^{++}\pi^-$ (π_2^+) events in which the slow pion indicated in brackets was undetected. Fortunately, the angular variation of the acceptance was rather smooth for reaction (5), where angular distributions were studied with events of $+++$ topology only. Results are given for this channel too.

We have fitted the angular distributions using the known theoretical dependences on the angles θ, o in the Δ_f^{++} and ρ^0 (ω, f_2, ρ_3^0) Jackson frames:

(i) for the Δ_f^{++}:

$$W_\Delta(\cos\theta) = \frac{3}{2}\left[\rho_{11}\left(\frac{1}{3} + \cos^2\theta\right) + \rho_{33}\sin^2\theta\right]$$

$$W_\Delta(o) = \frac{1}{2\pi}\left(1 - \frac{4}{\sqrt{3}} Re\rho_{3-1}\cos 2\phi\right)$$

where $\rho_{11} + \rho_{33} = 1/2$.

(ii) for the ρ^0 and ω mesons:

$$W_\rho(\cos\theta) = \frac{3}{4}\left(\rho_{00}\cos^2\theta + \rho_{11}\sin^2\theta\right)$$

$$W_\rho(\phi) = \frac{1}{2\pi}\left(1 - 2\rho_{1-1}\cos 2\phi\right)$$

with $\rho_{00} + 2\rho_{11} = 1$,

(iii) in the case of f_2 meson:

$$W_{f_2}(\cos\theta) = \frac{15}{8}\left[3\rho_{00}\left(\cos^2\theta - \frac{1}{3}\right)^2 + 4\rho_{11}\sin^2\theta\cos^2\theta + \rho_{22}\sin^4\theta\right]$$

$$W_{f_2}(\phi) = \frac{1}{2\pi}\left[1 - 2\left(\rho_{1-1} + \sqrt{\frac{2}{3}}Re\rho_{20}\right)\cos 2\phi + 2\rho_{2-2}\cos 4\phi\right]$$

with $\rho_{00} + 2(\rho_{11} + \rho_{22}) = 1$

(iv) for the ρ_3^0:

$$\begin{aligned} W_{\rho_3}(\cos\theta) &= \frac{7}{2}\left[\frac{1}{4}\rho_{00}\cos^2\theta\left(3 - 5\cos^2\theta\right)^2 + \frac{3}{8}\rho_{11}\sin^2\theta\left(1 - 5\cos^2\theta\right)^2 + \right. \\ &\quad \left. + \frac{15}{4}\rho_{22}\sin^4\theta\cos^2\theta + \frac{5}{8}\rho_{33}\sin^6\theta\right] \\ W_{\rho_3}(\phi) &= \frac{1}{2\pi}\left[1 - 2\left(\rho_{1-1} + \frac{2}{\sqrt{15}}Re\rho_{31} + \sqrt{\frac{6}{5}}Re\rho_{20}\right)\cos 2\phi + \right. \\ &\quad \left. + 2\left(\rho_{2-2} + \frac{2}{\sqrt{15}}Re\rho_{3-1}\right)\cos 4\phi - 2\rho_{3-3}\cos 6\phi\right] \end{aligned}$$

where $\rho_{00} + 2(\rho_{11} + \rho_{22} + \rho_{33}) = 1$.

The density matrix elements found both for the Δ_f^{++} and for the mesons in the reactions (2)-(5) are shown in Table 2.

Our results concerning the ρ^0 and f_2 density matrix elements show broad agreement with those measured at lower momenta (8, 9 and 12 GeV/c) in π^-p interactions [6,10], except for the ρ_{00} matrix element for the f_2, which we find to be definitely lower than found in [6,10], and for ρ_{1-1} for the ρ^0, which we find higher than [6,10].

The Δ_f^{++} density matrix elements were not measured in [6,9,10]. The results of [6] and [9] indicate however isotropy of Δ_f^{++} decay (i.e. $\rho_{11} = \rho_{33}$). Isotropic decay is not ruled out by the authors of [10]. Our results as shown in Table 2 show a distinctly different pattern, with high helicity of the Δ_f^{++} prevailing in both reactions.

7. Conclusions

The production of quasi-two-body final states via baryon exchange has been studied at 20 GeV/c. The reactions $\pi^+p \to p_f\pi^+\pi^+\pi^-$, $\pi^+p \to p_f\pi^+\pi^+\pi^-\pi^0$ and $\pi^+p \to \pi_f\pi^+\pi^0$ were identified in the WA56 data obtained at the CERN Ω spectrometer. The production of the $\rho_3^0(1690)$ state is observed for the first time in a baryon exchange reaction.

From our analysis we conclude that:

(i) The production of higher mass meson resonances is more prominent than it is for the ρ^0 meson, the cross section increasing nearly proportionally to M^2.

(ii) The energy dependence of the total backward cross sections in the $\Delta_f^{++}\rho^0$ and $\Delta_f^{++}f_2$ channels, where appropriate data at lower energy exist, shows the expected fast fall-off with energy ($\sigma \propto s^{-3.5}$).

(iii) The resonance decay angular distributions demonstrate that the diagonal elements of the density matrices which correspond to the lowest projection of spin dominate in the $\Delta_f^{++}\rho_3^0$ channel, but not in the $\Delta_f^{++}\rho^0$ and Δ_f^{++} f_2 channels.

Acknowledgements

We are indebted to the WA56 Collaboration for allowing us to analyse the data of their experiment. Three of us (N.Z.A., A.A.G. and V.V.K.) would like to express their gratitude to the CERN administration for kind hospitality and especially to the staff of the DD computing centre for continual help. A.A.G. and V.F.P. thank K.G. Boreskov, N.Ya. Ivanov, A.B. Kaidalov, and V.L. Morgunov for many useful discussions. Finally, we are grateful to Mme R. Audria for her patient assistance in the preparation of this paper.

References

[1] J.K. Storrow, Phys. Rep. 103 (1984) 317.

[2] W. Beusch, The Omega Prime Project. CERN-SPSC/77-70/T17.

[3] Z. Ajaltouni *et al.*, Nucl. Phys. B209 (1982) 301.

[4] J.-C. Lassalle *et al.*, Nucl. Instr. and Methods 176 (1980) 371.

[5] PDG, Review of Particle Properties, Phys. Lett. 239B (1990) 1.

[6] A. Ferrer *et al.*, Nucl. Phys. B142 (1978) 77.

[7] A. Rougé *et al.*, Phys.Lett. 69B (1977) 115.

[8] L. Montanet and G.C. Rossi, Phys.Rep. 63 (1980) 149

[9] A.V. Aref'ev *et al.*, Yad. Fiz. 51 (1990) 414.

[10] A. Abashian *et al.*, Phys. Rev. D13 (1976) 5.

Table Captions

Table 1. Number of prongs, number of events, acceptance, integral backward cross section and slope in u' for reactions (1)−(5).

Table 2. Density matrix elements.

Figure Captions

Fig. 1) The layout of the Ω spectrometer as used in the WA56 experiment.

Fig. 2) Contours of 90%, 70%, 50% and 30% geometrical acceptances of the Δ_f^{++} in the u' ($\pi^+ \rightarrow \Delta_f^{++}$) versus M_X^2 plane for the reaction $\pi^+ p \rightarrow \Delta_f^{++}$ X. The acceptance curves are computed supposing that the Δ_f^{++} is produced uniformly along the hydrogen target. The straight lines correspond to fixed values of Δ_f^{++} momentum.

Fig. 3) MM^2 distributions for $\pi^+ p \rightarrow p_f \pi^+ \pi^\pm$(MM)hypothesis for 3-prong events: a) $+++$ sample and b) $++-$ sample. The dashed vertical lines give the MM^2 limits of accepted events as input to the kinematics fitting program.

Fig. 4) MM^2 distributions for 3-prong events with the missing momentum extrapolating to the fired barrel element: a) $+++$ sample, b) $++-$ sample. The dashed vertical lines give the MM^2 limits of accepted events as input to the kinematics fitting program.

Fig. 5) Scatter plot $M(p_f \pi_1^+)$ versus $M(\pi_2^+ \pi^-)$, for 3-prong samples satisfying the corresponding 1-C kinematics.

Fig. 6) Projections of the scatter plot of Fig. 5: invariant $p_f \pi_1^+$ (a) and $\pi_2^+ \pi^-$ (b) mass spectra. The curves are the mass fit results explained in the text.

Fig. 7) Identification of effective 2-body channels: a) invariant $\pi_2^+ \pi^-$ mass spectrum recoiling from $\Delta_f^{++}(1232)$; b) invariant $\pi_2^+ \pi^-$ mass spectrum recoiling from $p_f \pi_1^+$ masses lying outside the Δ_f^{++} region ($1.08 < M(p_f \pi_1^+) < 1.15$ GeV/c^2 and $1.31 < M(p_f \pi_1^+) < 1.40$ GeV/c^2). The curves are the mass fit results explained in the text.

Fig. 8) Identification of reaction $p_f\pi_1^+\pi_2^+\pi^-\pi^0$: a) MM^2 opposite to Δ_f^{++} for events of +++ topology with missing momentum not pointing towards a fired barrel element; b) invariant mass of π_2^+ M^- combination (see text); c) invariant mass of the $\pi_2^+\pi^-\pi^0$ system when the $p_f\pi_1^+$ mass lies in the $\Delta(1232)$ band.

Fig. 9) MM^2 distribution for $\pi^+p \to p_f\pi^+$ (MM) hypothesis for 2-prong events.

Fig. 10) The two-prong sample: a) invariant $p_f\pi^+$ mass spectrum for the 2-prong events; b) MM^2 distribution for $\pi^+p \to \Delta_f^{++}$ (MM).

Fig. 11) The distribution of MM^2 opposite to Δ_f^{++} for two prong events with p_f momentum greater than 17 GeV/c. The arrow indicates the π^0 missing mass bump.

Fig. 12) Reaction amplitudes: a) the diagram describing the production of meson (M^*) and baryon (B^*) states via baryon exchange in πN reactions; b) the dual quark diagram which corresponds to two-quark state backward production; c) the dual quark diagram which corresponds to the production of baryon states. The dashed lines represent the string junctions.

Fig. 13) Compilation of backward total cross sections as function of incident π momentum for the reactions: $\pi^+p \to \Delta_f^{++}\rho^0$ (a), and $\pi^+p \to \Delta_f^{++}f_2$ (b). Black squares: our data. Circles: data of ref. [9]. Triangles: data of refs. [6,10], corrected as explained in the text.

Fig. 14) Differential cross sections of reactions $\pi^+p \to \Delta_f^{++}\pi^0$ (a), $\pi^+p \to \Delta_f^{++}\rho^0$ (b), $\pi^+p \to \Delta_f^{++}\omega$ (c), $\pi^+p \to \Delta_f^{++}f_2$ (d), and $\pi^+p \to \Delta_f^{++}\rho_3^0$ (e).

Table 1: Number of prongs, number of events, acceptance, integral backward cross section and slope in u' for reactions (1)–(5).

Reaction	Number of prongs	Number of events (background substracted)	Acceptance (%)	σ_{back} (nb)	Slope b $(GeV/c)^{-2}$
$\Delta_f^{++}\pi^0$	2	65 ± 20	4.0	18 ± 6	5.8 ± 0.6
$\Delta_f^{++}\rho^0(770)$	3	120 ± 16	3.3	29 ± 5	3.6 ± 0.5
$\Delta_f^{++}\rho^0(770)$	2	380 ± 80	15.0	28 ± 6	–
$\Delta_f^{++}f_2^0(1270)$	3	270 ± 26	5.3	75± 8	2.9± 0.3
$\Delta_f^{++}\rho_3^0(1690)$	3	180 ± 22	5.0	124 ± 18	2.5±0.3
$\Delta_f^{++}\omega$ (783)	4	7 ± 3	0.7	9 ± 4	–
$\Delta_f^{++}\omega$ (783)	3, +++ only	48 ± 10	3.6	12 ± 3	3.4 ± 0.6

Table 2: Density matrix elements

Reaction (2)	$\pi^+ p \to \Delta_f^{++} \rho^0$	
Δ_f^{++}	$\rho_{11} = -0.02 \pm 0.10$	$Re\rho_{3-1} = 0.05 \pm 0.11$
	$\rho_{33} = 0.52 \pm 0.10$	
ρ^0	$\rho_{00} = 0.19 \pm 0.16$	$\rho_{1-1} = 0.32 \pm 0.12$
	$\rho_{11} = 0.40 \pm 0.08$	
Reaction (3)	$\pi^+ p \to \Delta_f^{++} f_2$	
Δ_f^{++}	$\rho_{11} = 0.15 \pm 0.05$	$Re\rho_{3-1} = 0.07 \pm 0.05$
	$\rho_{33} = 0.35 \pm 0.05$	
f_2	$\rho_{00} = 0.08 \pm 0.07$	$\rho_{11} + \sqrt{2/3} Re\rho_{20} = -0.09 \pm 0.06$
	$\rho_{11} = 0.29 \pm 0.04$	$\rho_{2-2} = -0.03 \pm 0.07$
	$\rho_{22} = 0.17 \pm 0.04$	
Reaction (4)	$\pi^+ p \to \Delta_f^{++} \rho_3^0$	
Δ_f^{++}	$\rho_{11} = 0.37 \pm 0.07$	$Re\rho_{3-1} = -0.07 \pm 0.08$
	$\rho_{33} = 0.13 \pm 0.07$	
ρ_3^0	$\rho_{00} = 0.40 \pm 0.11$	$\rho_{1-1} + 2/\sqrt{15} Re\rho_{31} + \sqrt{6/5} Re\rho_{20} =$
	$\rho_{11} = 0.26 \pm 0.05$	$= -0.14 \pm 0.08$
	$\rho_{22} = -0.02 \pm 0.06$	$\rho_{2-2} + 2/\sqrt{15} Re\rho_{3-1} = -0.13 \pm 0.08$
	$\rho_{33} = 0.06 \pm 0.05$	$\rho_{3-3} = 0.10 \pm 0.08$
Reaction (5)	$\pi^+ p \to \Delta_f^{++} \omega$	
Δ_f^{++}	$\rho_{11} = 0.12 \pm 0.07$	$Re\rho_{3-1} = 0.12 \pm 0.07$
	$\rho_{33} = 0.38 \pm 0.07$	
ω	$\rho_{00} = 0.45 \pm 0.09$	$\rho_{1-1} = 0.02 \pm 0.06$
	$\rho_{11} = 0.27 \pm 0.05$	

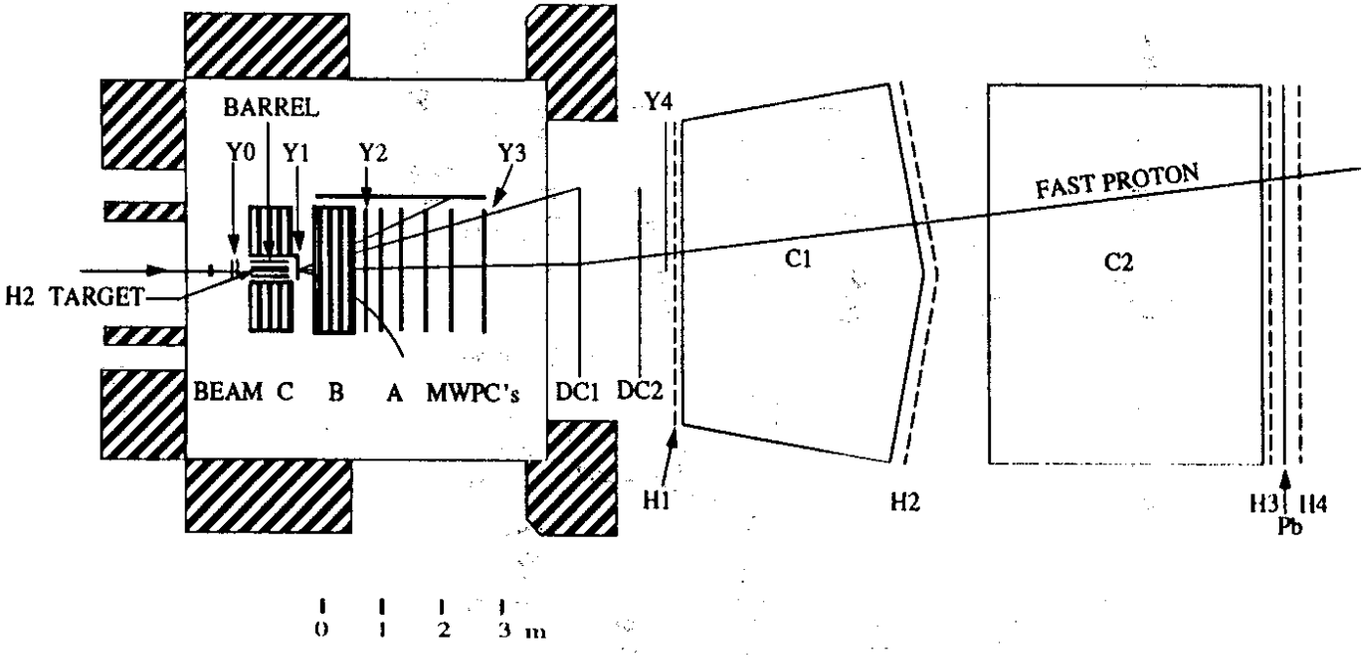
BARREL
Y0
Y1
Y2
Y3
Y4
FAST PROTON
H2 TARGET
C1
C2
BEAM C
B
A
MWPC's
DC1
DC2
H1
H2
H3
H4
Pb
0
1
2
3 m

FIG. 1

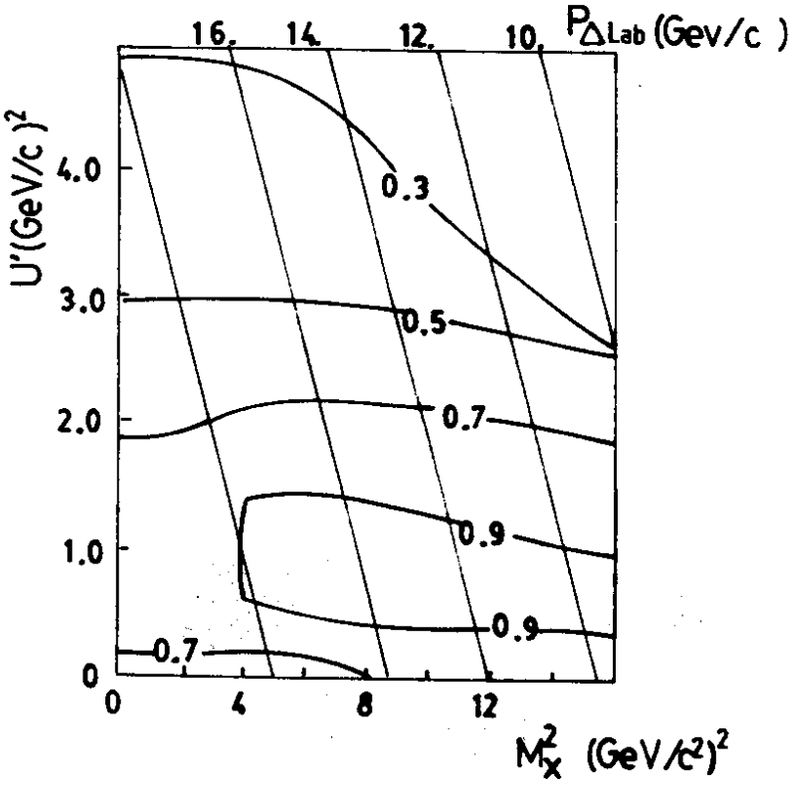
16.
14.
12.
10.
$P_{\Delta Lab}$ (Gev/c)
$U'(GeV/c)^2$
4.0
3.0
2.0
1.0
0
0.3
0.5
0.7
0.9
0.9
0.7
0
4
8
12
M_x^2 $(GeV/c^2)^2$

FIG. 2

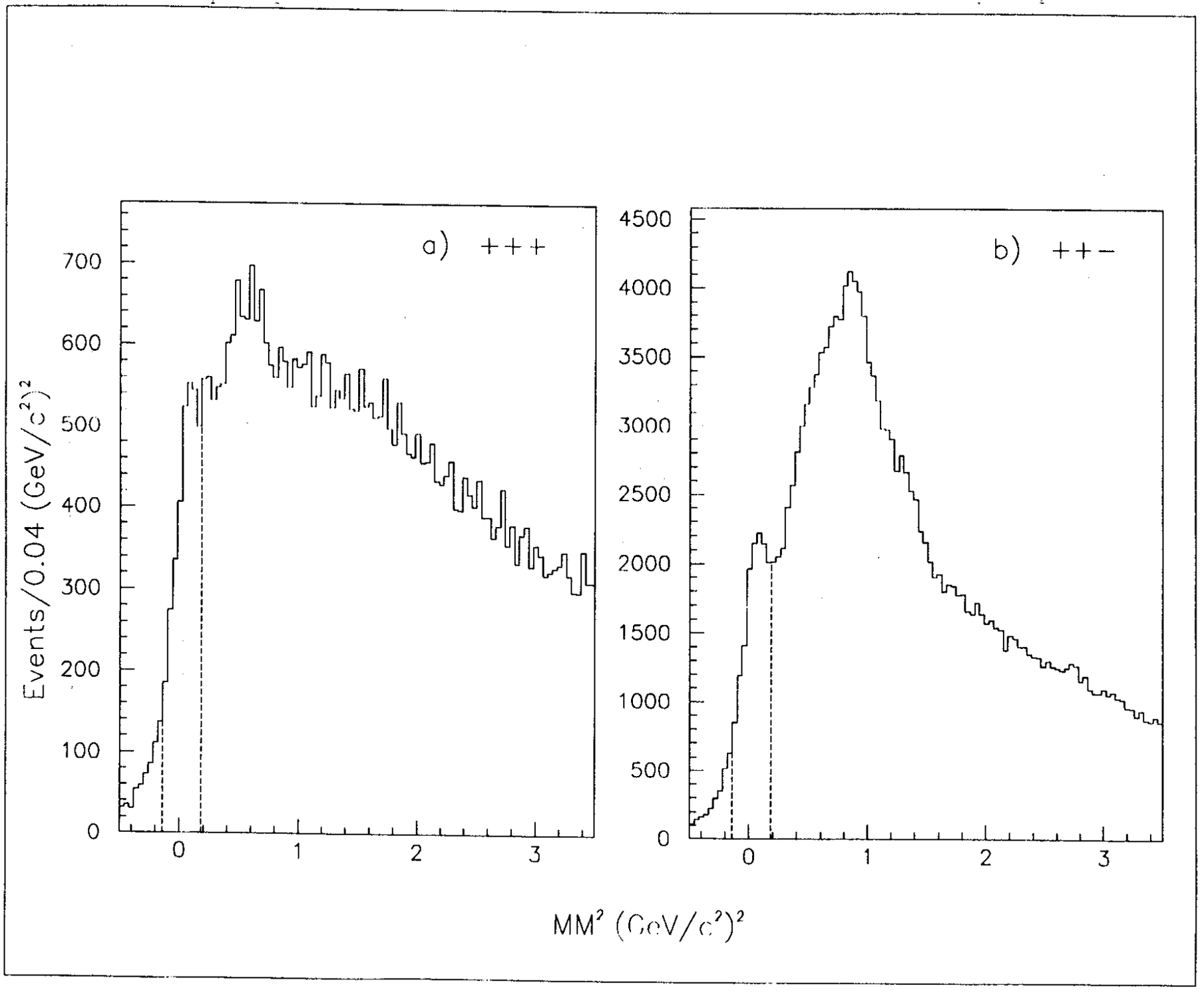
a) +++
b) ++−
Events/0.04 (GeV/c²)²
MM² (GeV/c²)²
0
100
200
300
400
500
600
700
500
1000
1500
2000
2500
3000
3500
4000
4500
0
1
2
3

FIG. 3

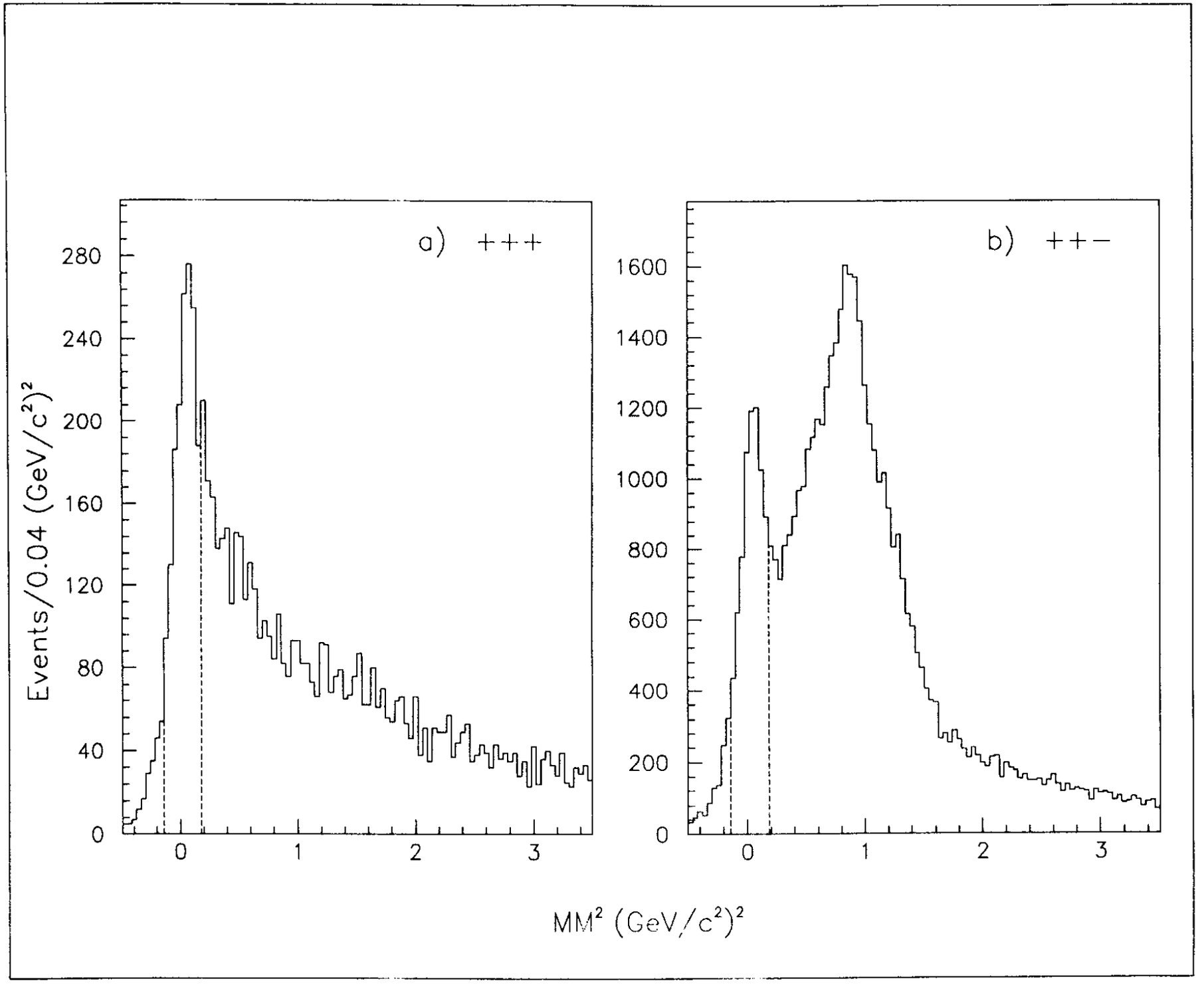
a) +++
b) ++−
Events/0.04 (GeV/c²)²
MM² (GeV/c²)²
0
40
80
120
160
200
240
280
200
400
600
800
1000
1200
1400
1600
0
1
2
3

FIG. 4

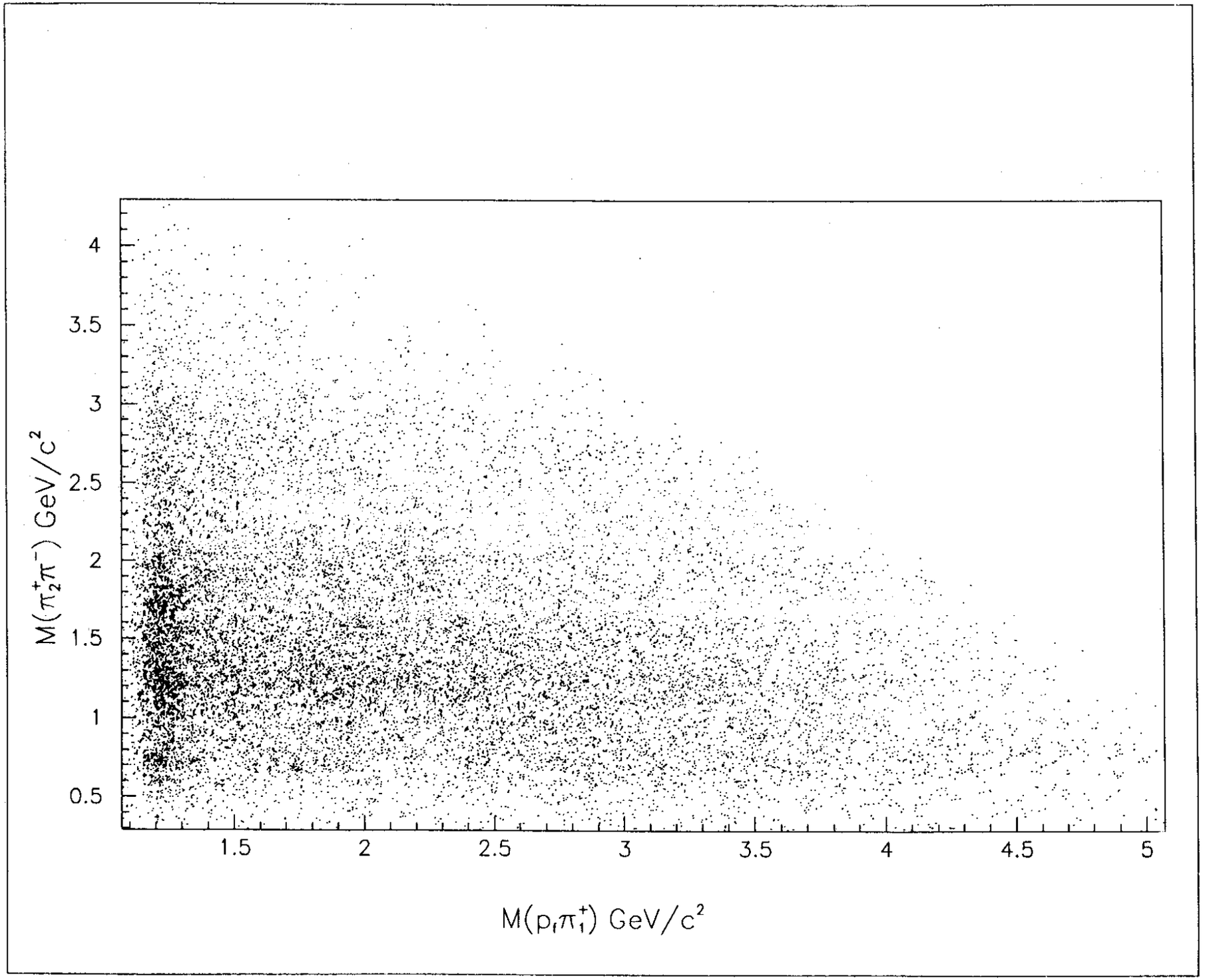

FIG. 5

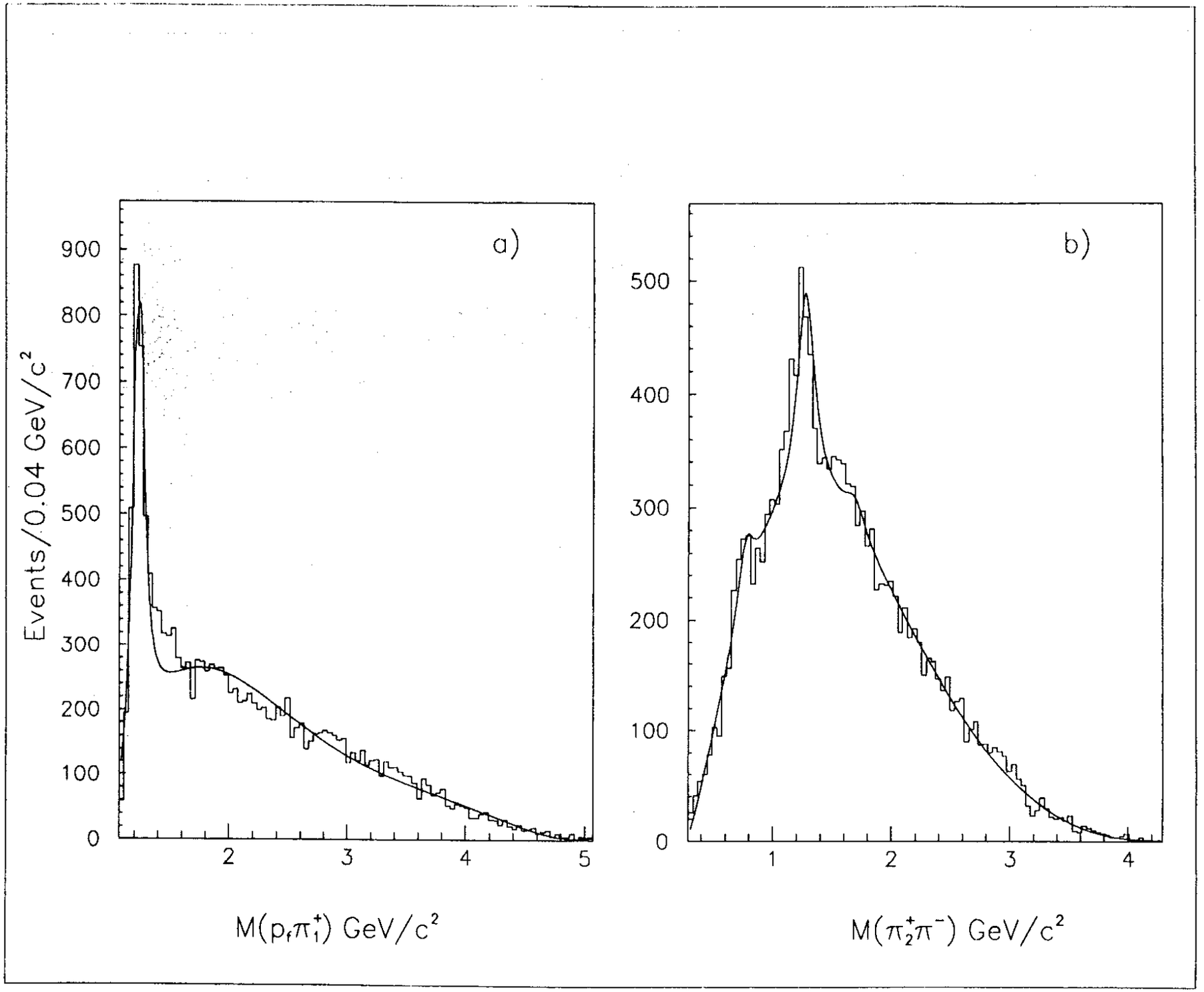
a)
b)
Events/0.04 GeV/c²
M(p_f π₁⁺) GeV/c²
M(π₂⁺π⁻) GeV/c²
0
100
200
300
400
500
600
700
800
900
1
2
3
4
5

FIG. 6

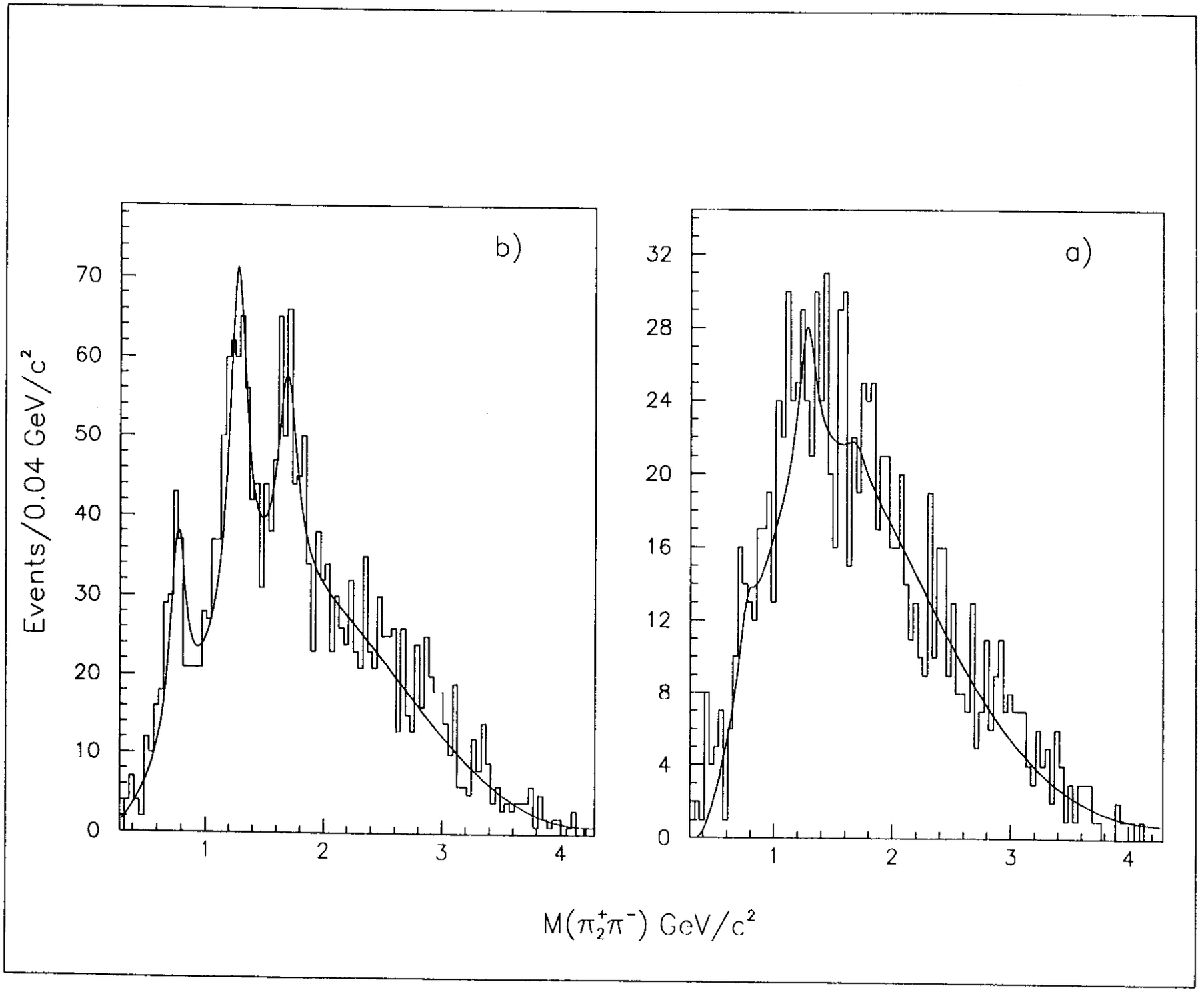
b)
a)
Events/0.04 GeV/c²
M(π₂⁺π⁻) GeV/c²
0
10
20
30
40
50
60
70
4
8
12
16
20
24
28
32
1
2
3
4

FIG. 7

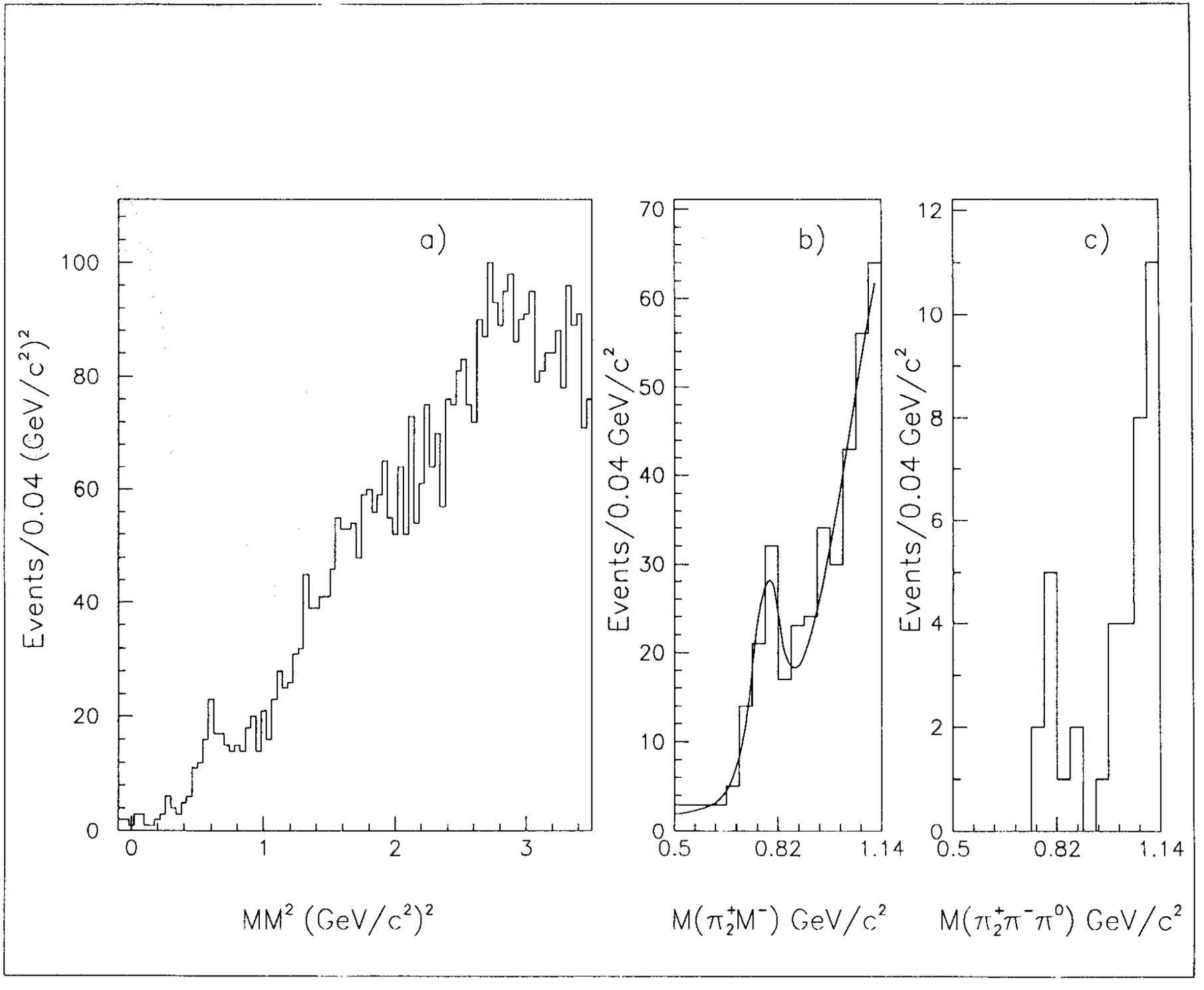
a)
b)
c)
Events/0.04 (GeV/c²)²
Events/0.04 GeV/c²
Events/0.04 GeV/c²
MM² (GeV/c²)²
M(π₂⁺M⁻) GeV/c²
M(π₂⁺π⁻π⁰) GeV/c²
0
20
40
60
80
100
10
30
50
70
2
4
6
8
10
12
0.5
0.82
1.14
1
2
3

FIG. 8

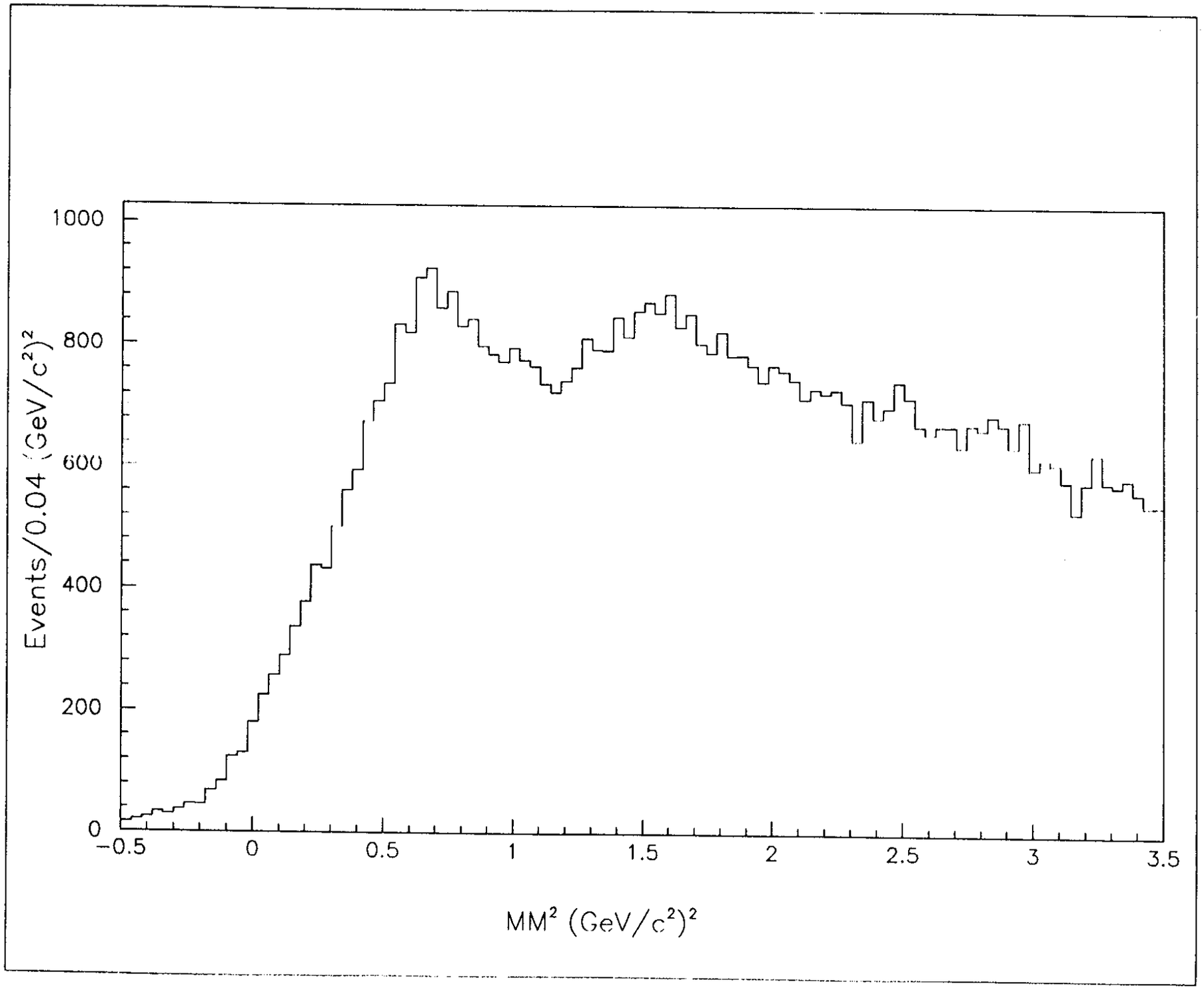
1000
800
600
400
200
0
Events/0.04 (GeV/c²)²
−0.5
0
0.5
1
1.5
2
2.5
3
3.5
MM² (GeV/c²)²

FIG. 9

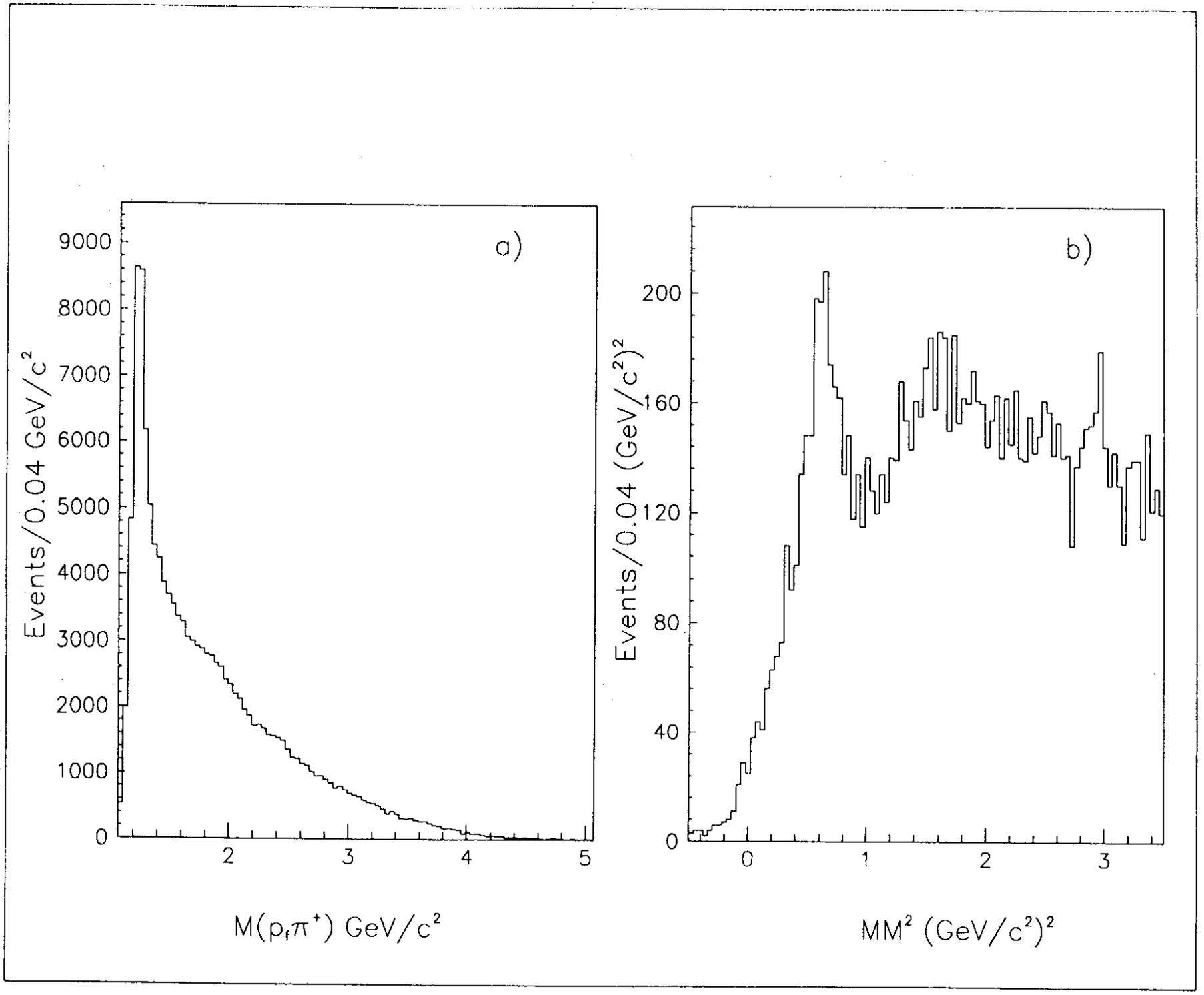
a)
b)
Events/0.04 GeV/c²
Events/0.04 (GeV/c²)²
M(p_f π⁺) GeV/c²
MM² (GeV/c²)²
0
1000
2000
3000
4000
5000
6000
7000
8000
9000
40
80
120
160
200
1
2
3
4
5

FIG. 10

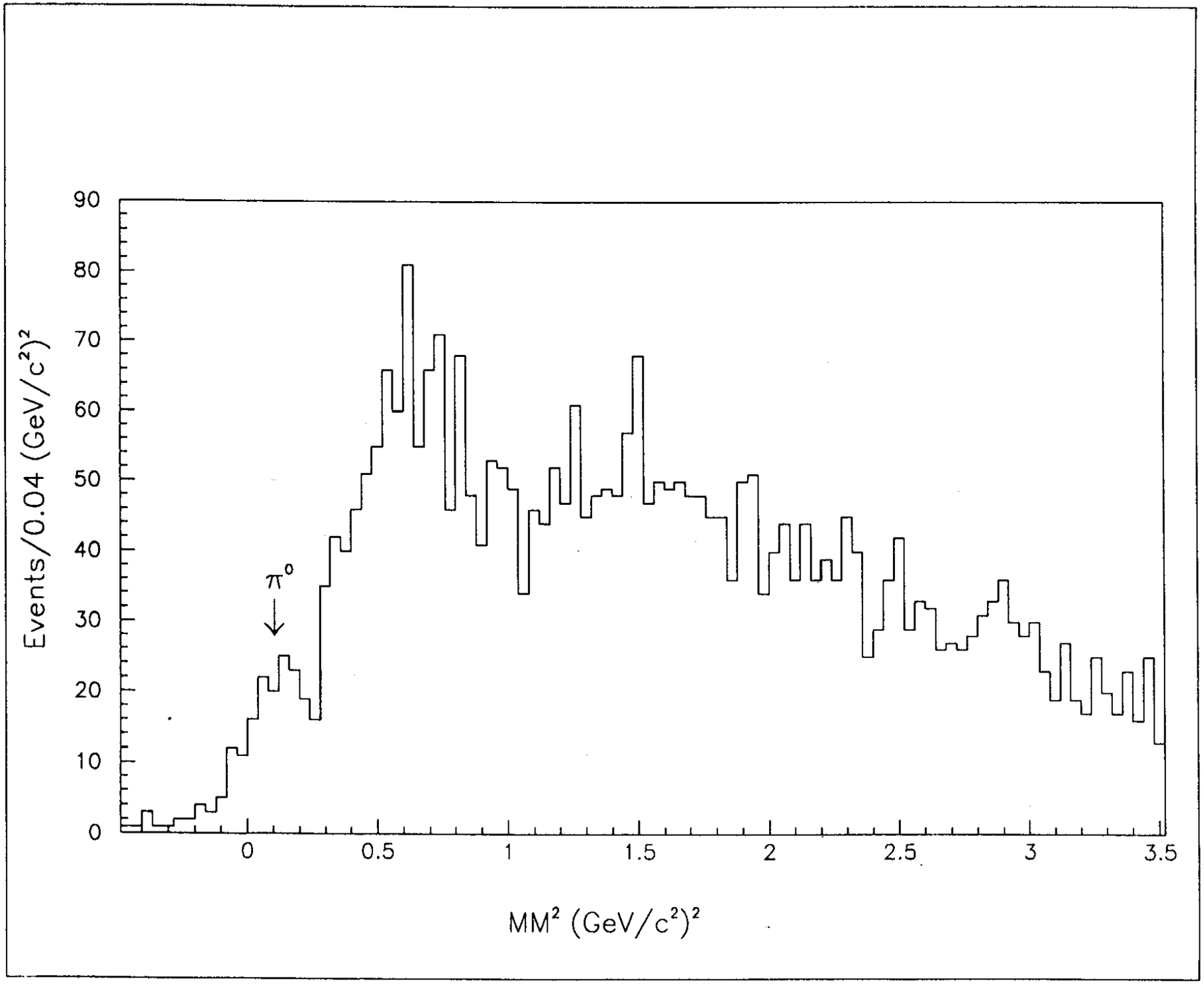
90
80
70
60
50
40
30
20
10
0
Events/0.04 (GeV/c²)²
π°
0
0.5
1
1.5
2
2.5
3
3.5
MM² (GeV/c²)²

FIG. 11

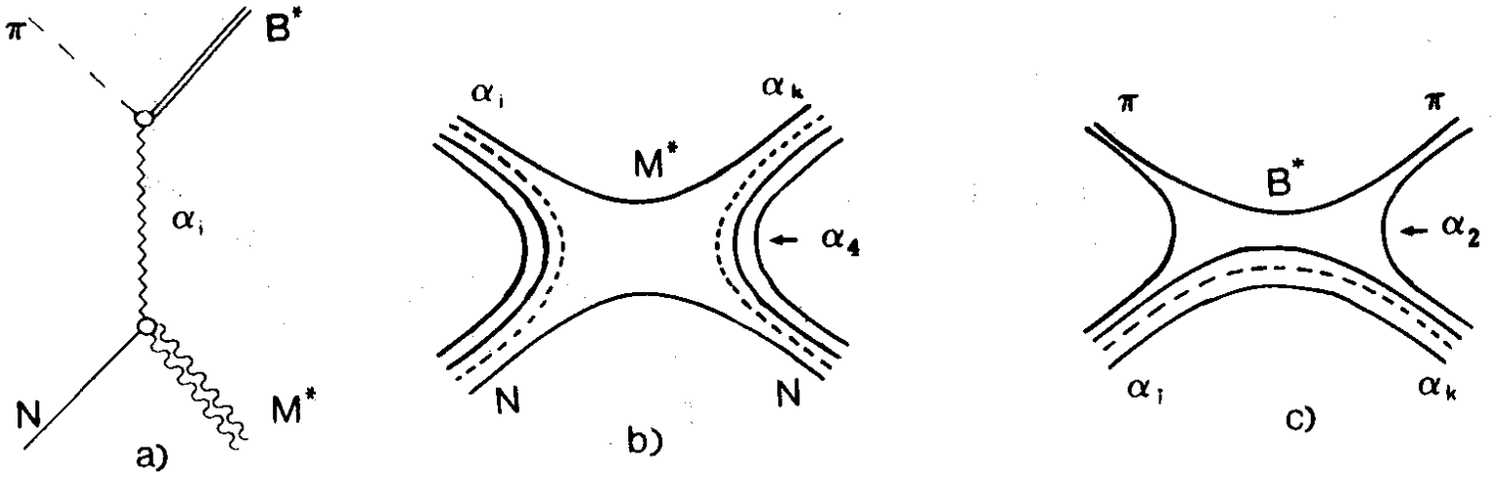

FIG. 12

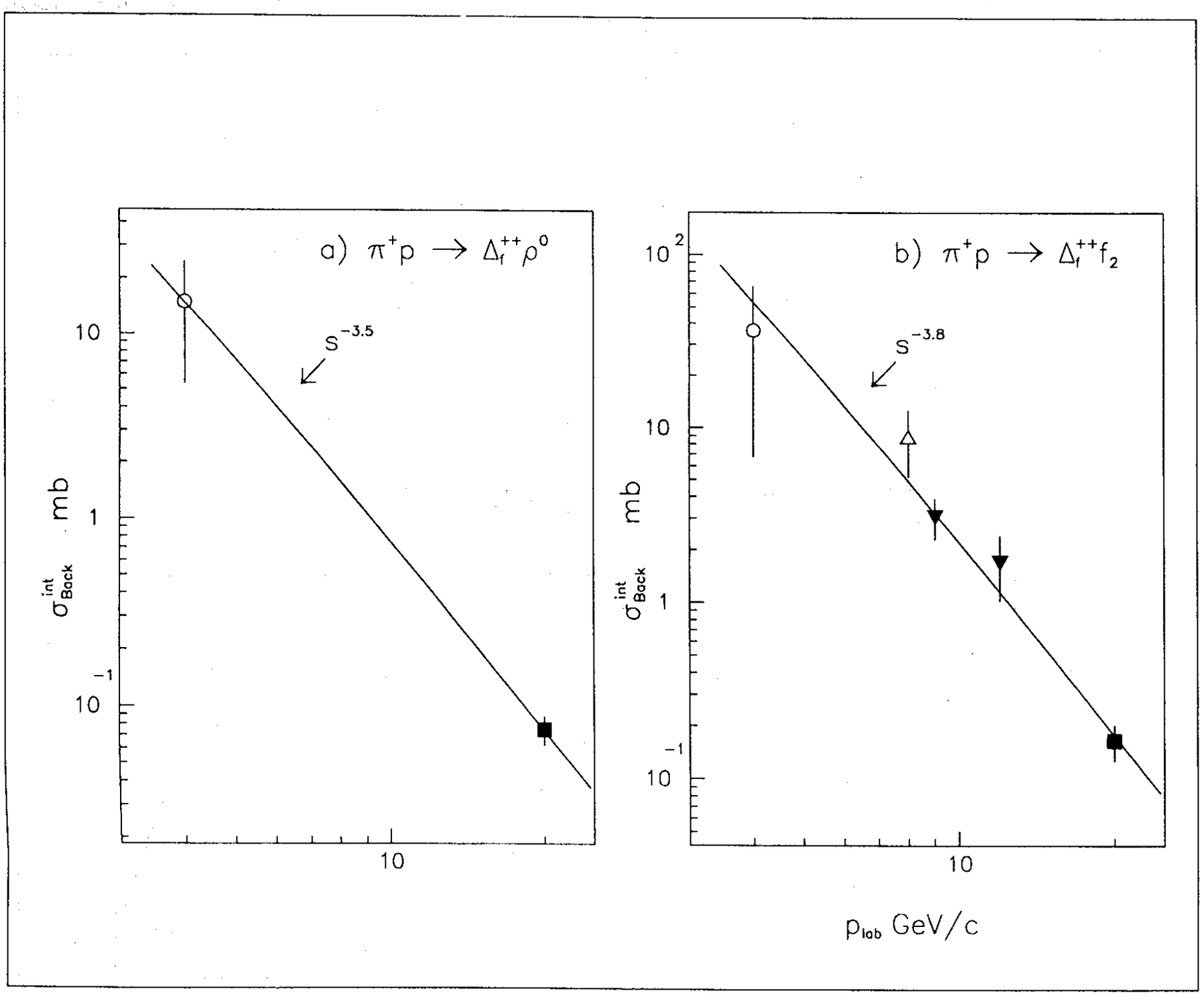
a) $\pi^+ p \rightarrow \Delta_f^{++} \rho^0$
$s^{-3.5}$
σ^{int}_{Back} mb
10
1
10^{-1}
10
b) $\pi^+ p \rightarrow \Delta_f^{++} f_2$
$s^{-3.8}$
10^2
10
1
10^{-1}
10
p_{lab} GeV/c

FIG. 13

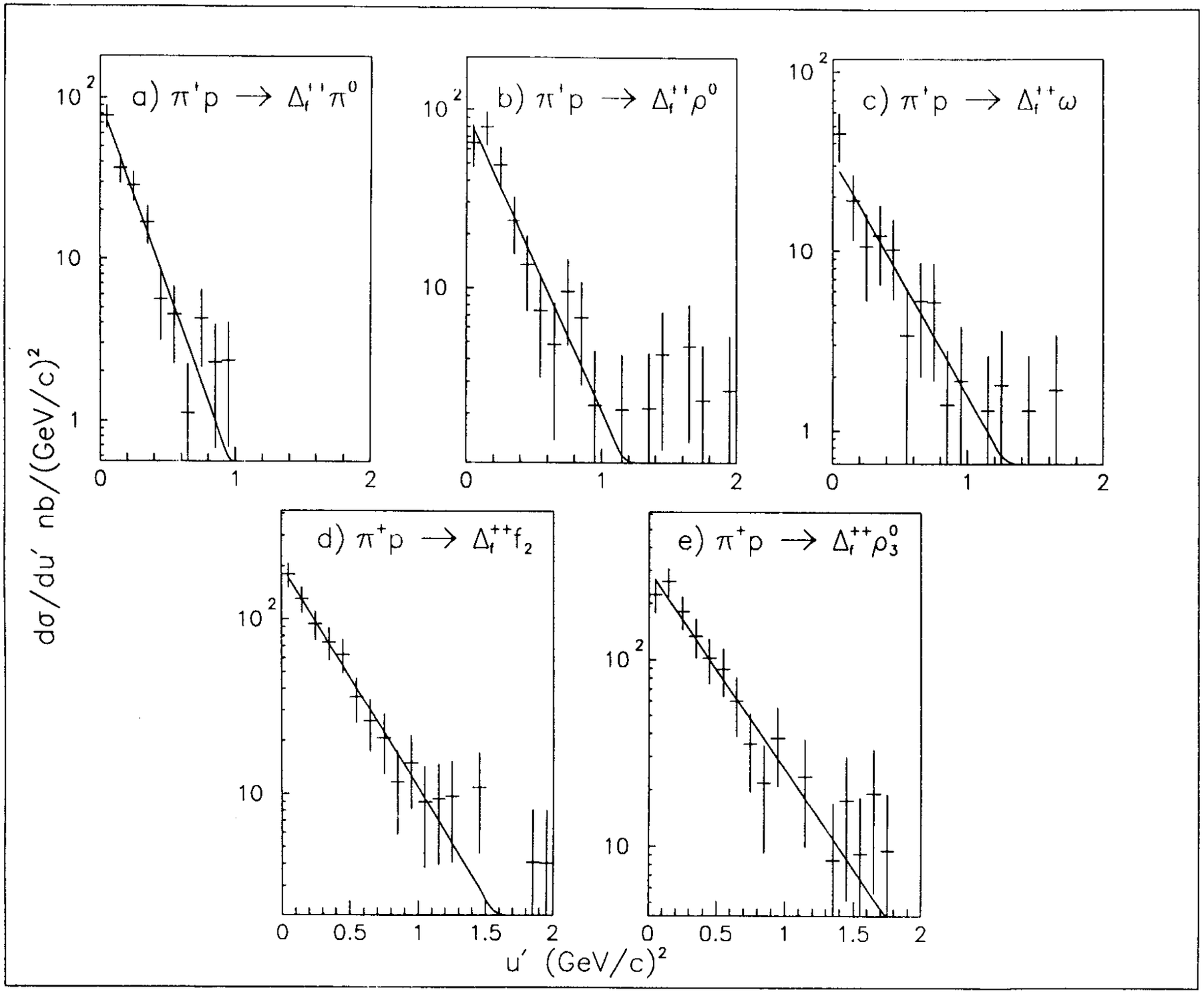

FIG. 14

Imprimé au CERN. Prix : 0.90 Fr.